

Ghost Imaging of Dark Particles

J. Estrada[⊗],¹ R. Harnik[∠],¹ D. Rodrigues[✉],^{2,1} and M. Senger[✉],^{2,3}

¹*Fermi National Accelerator Laboratory, PO Box 500, Batavia IL, 60510, USA*

²*Department of Physics, FCEN, University of Buenos Aires and IFIBA, CONICET, Buenos Aires, Argentina*

³*Physik-Institut der Universität Zürich*

(Dated: October 31, 2020)

We propose a new way to use optical tools from quantum imaging and quantum communication to search for physics beyond the standard model. Spontaneous parametric down conversion (SPDC) is a commonly used source of entangled photons in which pump photons convert to a signal-idler pair. We propose to search for “dark SPDC” (dSPDC) events in which a new dark sector particle replaces the idler. Though it does not interact, the presence of a dark particle can be inferred by the properties of the signal photon. Examples of dark states include axion-like-particles and dark photons. We show that the presence of an optical medium opens the phase space of the down-conversion process, or decay, which would be forbidden in vacuum. Search schemes are proposed which employ optical imaging and/or spectroscopy of the signal photons. The signal rates in our proposal scales with the second power of the feeble coupling to new physics, as opposed to light-shining-through-wall experiments whose signal scales with coupling to the fourth. We analyze the characteristics of optical media needed to enhance dSPDC and estimate the rate. A bench-top demonstration of a high resolution ghost imaging measurement is performed employing a Skipper-CCD to demonstrate its utility in a dSPDC search.

I. INTRODUCTION

Nonlinear optics is a powerful new tool for quantum information science. Among its many uses, it plays an enabling role in the areas of quantum networks and teleportation of quantum states as well as in quantum imaging. In quantum teleportation [1–4] the state of a distant quantum system, Alice, can be inferred without directly interacting with it, but rather by allowing it to interact with one of the photons in an entangled pair. The coherence of these optical systems has recently allowed teleportation over a large distance [5]. Quantum ghost imaging, or “interaction-free” imaging [6], is used to discern (usually classical) information about an object without direct interaction. This technique exploits the relationship among the emission angles of a correlated photon pair to create an image with high angular resolution without placing the subject Alice in front of a high resolution detector or allowing it to interact with intense light. These methods of teleportation and imaging rely on the production of signal photons in association with an idler pair which is entangled (or at least correlated) in its direction, frequency, and sometimes polarization.

Quantum ghost imaging and teleportation both differ parametrically from standard forms of information transfer. This is because a system is probed, not by sending information to it and receiving information back, but rather by sending it half of an EPR pair, without need for a “response”. The difference is particularly apparent if Alice is an extremely weakly coupled system, say she is part of a dark sector, with a coupling ϵ to photons. The rate of information flow

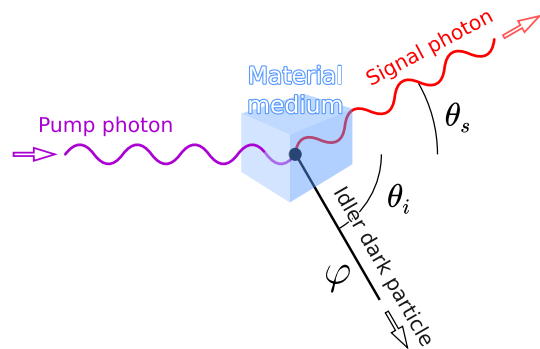


Figure 1: Pictorial representation of the dSPDC process. A dark particle φ is emitted in association with a signal photon. The presence of φ can be inferred from the distribution of the signal photon in angle and/or frequency. We consider both the colinear ($\theta_s = 0$) and non-colinear ($\theta_s \neq 0$) cases.

in capturing an image of Alice will occur at a rate $\propto \epsilon^4$ with standard methods, but at a rate $\propto \epsilon^2$ using quantum optical methods.

A common method for generating entangled photon pairs is the nonlinear optics process known as *spontaneous parametric down conversion* (SPDC). In SPDC a pump photon decays, or down-converts, within a nonlinear optical medium into two other photons, a signal and an idler. The presence of the SPDC idler can be inferred by the detection of the signal [7]. SPDC is in wide use in quantum information and provides the seed for cavity enhanced setups such as optical parametric oscillators (OPO) [8].

In this work we propose to use quantum imaging and quantum communication tools to perform an interaction-free search for the emission of new particles beyond the standard model. The new tool we present is *dark SPDC*, or dSPDC, an example sketch of which is shown in Figure 1. A pump photon enters an optical medium and down-converts to a signal pho-

[⊗] estrada@fnal.gov

[∠] roni@fnal.gov

[✉] rodriguesfm@df.uba.ar

[✉] matias.senger@physik.uzh.ch

ton and a dark particle, which can have a small mass, and does not interact with the optical medium. Like SPDC, in dSPDC the presence of a dark state can be inferred by the angle and frequency distribution of the signal photon that was produced in association. The dSPDC process can occur either collinearly, with $\theta_s = \theta_i = 0$, or as shown in the sketch, in a non-collinear way.

The new dark particles which we propose to search for, low in mass and feebly interacting, are simple extensions of the standard model (SM). Among the most well motivated are axions, or axion-like-particles, and dark photons (see [9] for a review). Since these particles interact with SM photons, optical experiments provide an opportunity to search for them. A canonical setup is light-shining-through-wall (LSW) which set interesting limits on axions and dark photons using optical cavities [10]. In optical LSW experiments a laser photon converts to an axion or dark photon, enabling it to penetrate an opaque barrier. For detection, however, the dark state must convert back to a photon and interact, which is a rare occurrence. As a result, the signal rate in LSW scales as ϵ^4 , where ϵ is a small coupling to dark states. This motivates the interaction-free approach of dSPDC, in which the dark state is produced but does not interact again, yielding a rate $\propto \epsilon^2$.

From the perspective of particle physics, dSPDC, and also SPDC, may sound unusual¹. In dSPDC, for example, a massless photon is decaying to another massless photon plus a massive particle. In the language of particle physics this would be a kinematically forbidden transition. The process, if it were to happen in vacuum, violates energy and momentum conservation and thus has no available phase space. In this paper we show how optics enables us to perform “engineering in phase space” and open kinematics to otherwise forbidden channels. This, in turn, allows to design setups in which the dSPDC process is allowed and can be used to search for dark particles.

Broadly speaking, the search strategies we propose may be classified as employing either imaging or spectroscopic tools, though methods employing both of these are also possible. In the first, the angular distribution of signal photons are measured, and in the second, the energy distribution is observed. For an imaging based search, a high angular resolution is required, while the spectroscopic approach requires high frequency resolution. The later has the benefit that dSPDC can be implemented in a waveguide which will enhance its rate for long optical elements [16, 17].

We present the basic ideas and formalism behind this method, and focus on the phase space for dSPDC. We compare the phase space distributions of SPDC to dSPDC and discuss factors which may enhance the rate of dSPDC processes. To estimate the dSPDC rates in this work we re-scale known SPDC results. In a companion paper [17] we will derive the dSPDC

rate more carefully, focusing on the spectroscopic approach and on *collinear* dSPDC in bulk crystals and waveguides.

In this work we also present a proof-of-concept experiment using a quantum imaging setup with a Skipper CCD [18]. The high resolution is shown to produce a high resolution and low noise angular image of an SPDC pattern. Such a detector may be employed both in imaging and spectroscopic dSPDC setups.

This paper is structured as follows. In Section II we review axion-like particles and dark photons and present their Hamiltonians in the manner they are usually treated in nonlinear optics. In Section III we discuss energy and momentum conservation, which are called *phase matching conditions* in nonlinear optics, and the phase space for dSPDC. The usual conservation rules will hold exactly in a thought experiment of an infinite optical medium. In Section III C we discuss how the finite size of the optical medium broadens the phase space distribution and plot it as a function of the signal photon angle and energy. In Section IV we discuss the choice of optical materials that allow for the dSPDC phase matching to enhance its rates and to suppress or eliminate SPDC backgrounds. In Section V we discuss the rates for dSPDC and its scaling with the geometry of the experiment, showing potential promising results for collinear waveguide setups with long optical elements. In Section VI, we present an experimental proof-of-concept in which a Skipper CCD is used to image an SPDC pattern with high resolution. We discuss future directions and conclude in Section VII.

II. THE DARK SPDC HAMILTONIAN

The SPDC process can be derived from an effective nonlinear optics Hamiltonian of the form [19, 20]

$$\mathcal{H}_{\text{SPDC}} = \chi^{(2)} E_i E_s E_p \quad (1)$$

where E_j is the electric field for pump, signal, and idler photons and $j = p, s, i$ respectively. We adopt the standard notation in nonlinear optics literature in which the vector nature of the field is implicit. Thus the pump, signal and idler can each be of a particular polarization and $\chi^{(2)}$ represents the coupling between the corresponding choices of polarization.

We now consider the dark SPDC Hamiltonian

$$\mathcal{H}_{\text{dSPDC}} = g_\varphi \varphi E_s E_p \quad (2)$$

in which a pump and signal photon couple to a new field φ which has a mass m_φ . The effective coupling g_φ , depends on the model and can depend on the frequencies in the process, the polarizations and the directions of outgoing particles. This type of term arises in well motivated dark sector models including axion-like particles and dark photons.

A. Axion-like particles

Axion-like particles, also known as ALPs, are light pseudoscalar particles that couple to photons via a

¹ Searches for missing energy and momentum are a commonplace tool in the search for new physics at colliders [11–15]. However, the dSPDC kinematics are distinct as we show.

term

$$\mathcal{H}_{\text{axion}} = g_\varphi \varphi \vec{E} \cdot \vec{B}, \quad (3)$$

which can be written in the scalar form of Equation (2) with the pump and signal photons chosen to have orthogonal polarization. The coupling g_φ in this case is the usual axion-photon coupling $\sim 1/f_a$. ALPs are naturally light thanks to a spontaneously broken global symmetry at a scale f_a .

Since we will not perform a detailed analysis of backgrounds and feasibility here, we will describe existing limits on ALPs qualitatively and refer readers to limit plots in [9, 21]. In this work we will consider searches that can probe ALPs with a mass of order 0.1 eV or lower. Existing limits in this mass range come from stellar and supernova dynamics[22], as well as from the CAST Helioscope [23], which require $g_\varphi \lesssim 10^{-10} \text{ GeV}^{-1}$. For comparison with our setups, we will also consider limits that are entirely lab-based, which are much weaker. At $\sim 0.1 \text{ eV}$ ALP coupling of order 10^{-6} GeV^{-1} are allowed by all lab-based searches. For axion masses around $10^{-3} - 10^{-2} \text{ eV}$ the PVLAS search[24] for magnetic birefringence places a limit of $g_\varphi \lesssim 10^{-7} - 10^{-6} \text{ GeV}^{-1}$. Below masses of an meV, LSW experiments such as OSQAR [25] and ALPS [26] set $g_\varphi \lesssim 6 \times 10^{-8}$. A large scale LSW facility, ALPS II [27], is proposed in order to improve upon astrophysical limits and CAST.

B. Dark photons

A new U(1) gauge field, A' , with mass $m_{A'}$ that mixes kinetically with the photon via the Hamiltonian

$$\mathcal{H}_{\text{mix}} = \epsilon F^{\mu\nu} F'_{\mu\nu} = \epsilon (\vec{E} \cdot \vec{E}' + \vec{B} \cdot \vec{B}'). \quad (4)$$

It is possible to write the dark photon interaction in a basis in which any electromagnetic current couples to longitudinally polarized dark photons with an effective coupling of $\epsilon(m_{A'}/\omega_{A'})$ and to transversely polarized dark photons with $\epsilon(m_{A'}/\omega_{A'})^2$ [28, 29]. The same dynamics that leads to the nonlinear Hamiltonian $\mathcal{H}_{\text{SPDC}}$, will yield an effective coupling of two photons to a dark photon as in Equation (2) with φ representing a dark photon polarization state. For longitudinal polarization of the dark photon this can be brought to the form of equation (2) with $g_\varphi = \epsilon \chi^{(2)} m_\varphi$. The coupling to transverse dark photons will be suppressed by an additional factor of m_φ/ω_φ .

Like axions, limits on dark photons come from astrophysical systems, such as energy loss in the Sun [28], as well as the lack of a detection of dark photons emitted by the Sun in dark matter direct detection experiments [29]. At a dark photon mass of order 0.1 eV, the limit on the kinetic mixing is $\epsilon \lesssim 10^{-10}$ with the limit becoming weaker linearly as the dark photon mass decreases. Among purely lab-based experiments, ALPS sets a limit of $\epsilon \lesssim 3 \times 10^{-7}$. In forthcoming sections of this work we will use these limits as benchmarks.

◻◻◻◻

In addition to ALPs and dark photons, one can consider other new dark particles that are sufficiently light and couples to photons. Examples include millicharged particle, which can be produced in pairs in association with a signal photon. We leave these generalizations for future work and proceed to discuss the phase space for dSPDC in a model-independent way.

III. PHASE SPACE OF DARK SPDC

As stated above, the effective energy and momentum conservation rules in nonlinear optics are known as “phase matching conditions”. We begin by reviewing their origin to make the connection with energy and momentum conservation in particle physics and then proceed to solve them for SPDC and dSPDC, to understand the phase space for these processes.

A. Phase matching and particle decay

We begin with a discussion of the phase space in a two-body decay, or spontaneous down-conversion. We use particle physics language, but will label the particles as is usual in the nonlinear optics systems which we will be discussing from the onset. A pump particle p decays into a signal particle s and another particle, either an idler photon i or a dark particle φ :

$$\begin{aligned} \text{SPDC:} & \quad \gamma_p \rightarrow \gamma_s + \gamma_i \\ \text{dSPDC:} & \quad \gamma_p \rightarrow \gamma_s + \varphi. \end{aligned} \quad (5)$$

We would like to discuss the kinematics of the standard model SPDC process, and the BSM dSPDC process together, to compare and contrast. For this, in the discussion below we will use the idler label i to represent the idler photon in the SPDC case, and φ in the dSPDC case. Hence \mathbf{k}_i and θ_i are the momentum and emission angle of either the idler photon or of φ , depending on the process.

The differential decay rate in the laboratory frame is given by [21]

$$\frac{d\Gamma}{d^3k_s d^3k_i} = \frac{\delta^4(p_{p\mu} - p_{s\mu} - p_{i\mu})}{(2\pi)^2 2\omega_p 2\omega_s 2\omega_i} |\mathcal{M}|^2 \quad (6)$$

where \mathcal{M} is the amplitude for the process (which carries a mass dimension of +1), and the energy-momentum four-vectors

$$p_{j\mu} = \begin{pmatrix} \omega_j \\ \mathbf{k}_j \end{pmatrix} \quad (7)$$

with $j = p, s, i$. Traditionally, one proceeds by integrating over four degrees of freedom within the six dimensional phase space, leaving a differential rate with respect to the two dimensional phase space. This is often chosen a solid angle for the decay $d\Omega$, but in our case there will be non-trivial correlations of frequency and angle as we will see in the next subsection.

It is instructive, however, for our purpose to take a step back and recall how the energy-momentum conserving δ -functions come about. In calculating the

quantum amplitude for the transition, the fields in the initial and final states are expanded in modes. The plane-wave phases $e^{i(\omega t - \mathbf{k} \cdot \mathbf{x})}$ are collected from each and a spacetime integral is performed

$$\int d^4x e^{i(\Delta\omega t - \Delta\mathbf{k} \cdot \mathbf{x})} = (2\pi)^4 \delta^{(3)}(\Delta\mathbf{k}) \delta(\Delta\omega), \quad (8)$$

where frequency and momentum mismatch are defined as

$$\begin{cases} \Delta\omega = \omega_p - \omega_s - \omega_i \\ \Delta\mathbf{k} = \mathbf{k}_p - \mathbf{k}_s - \mathbf{k}_i \end{cases}, \quad (9)$$

and again, the label i can describe either an idler photon or a dark particle φ . In Equation (9), we separated momentum and energy conserving delta functions to pay homage to the optical systems which will be the subject of upcoming discussion. The squared amplitude $|\mathcal{M}|^2$, and hence the rate, is proportional to a single power of the energy-momentum conserving delta function times a space-time volume factor, which is absorbed for canonically normalized states (see e.g. [30]), giving Equation (6).

The message from this is that energy and momentum conservation, which are a consequence of Neother's theorem and space-time translation symmetry, is enforced in quantum field theory by perfect destructive interference whenever there is a non-zero mismatch in the momentum or energy of initial and final states. In this sense, the term “phase matching” captures the particle physicist's notion of energy and momentum conservation well.

The dSPDC process shown in Figure 1 is a massless pump photon decaying to a signal photon plus a massive particle φ . This process clearly cannot occur in vacuum. For example, if we go to the rest frame of φ , and define all quantities in this frame with a tilde $\tilde{}$, the conservation of momentum implies $\tilde{\mathbf{k}}_p = \tilde{\mathbf{k}}_s$, while the conservation of energy implies $\tilde{\omega}_p = \tilde{\omega}_s + m$. Combining these with the dispersion relation for a photon in vacuum $\tilde{\omega}_{p,s} = |\tilde{\mathbf{k}}_{p,s}|$, implies that energy and momentum conservation cannot be satisfied and the process is kinematically forbidden. Another way to view this is to recall that the energy-momentum four-vector for the initial state (a photon) lies on a light cone i.e. it is a null four-vector, $p^\mu p_\mu = 0$, while the final state cannot accomplish this since there is a nonzero mass.

In this work we show that optical systems will allow us to open phase space for dSPDC. When a photon is inside an optical medium a different dispersion relation holds,

$$\tilde{n}_p \tilde{\omega}_p = |\tilde{\mathbf{k}}_p| \quad \text{and} \quad \tilde{n}_s \tilde{\omega}_s = |\tilde{\mathbf{k}}_s| \quad (10)$$

where \tilde{n}_p and \tilde{n}_s are indices of refraction of photons in the medium in the φ rest frame, which can be different for pump and signal. As we will see later on, under these conditions the conclusion that $p \rightarrow s + \varphi$ is kinematically forbidden can be evaded.

Another effect that occurs in optical systems, but not in decays in particle physics, is the breaking of spatial translation invariance by the finite extent of the optical medium. This allows for violation of momentum conservation along the directions in which the

medium is finite. As a result, the sharp momentum conserving delta function will become a peaked distribution of width L^{-1} , where L is the crystal size. We will begin by solving the exact phase matching conditions in SPDC and dSPDC in the following subsection, which correspond to the phase space distributions for an infinitely large crystal. Next, we will move on to the case in which the optical medium is finite.

B. Phase Matching in dSPDC

We now study the phase space for dSPDC to identify the correlations between the emission angle and the frequency of the signal photon. We will consider in parallel the SPDC process as well, so in the end we arrive to both results. We assume in this subsection an optical medium with an infinite extent, such that the delta-functions enforce energy and momentum conservation.

The phase matching conditions $\Delta\omega = 0$ and $\Delta\mathbf{k} = 0$ —that must be strictly satisfied in the infinite extent optical medium scenario—imply

$$\begin{cases} \omega_p = \omega_s + \omega_i \\ \mathbf{k}_p = \mathbf{k}_s + \mathbf{k}_i \end{cases}. \quad (11)$$

Using the \mathbf{k} 's decomposition shown in Figure 1 the second equation can be expanded in coordinates parallel and perpendicular to the pump propagation direction

$$\begin{cases} k_p = k_s \cos \theta_s + k_i \cos \theta_i \\ 0 = k_s \sin \theta_s - k_i \sin \theta_i \end{cases} \quad (12)$$

where the angles θ_s and θ_i are those indicated in the cited figure. Since this process is happening in a material medium, the photon dispersion relation is $k = n\omega$ where n is the refractive index. The refractive index is in general a function of frequency, polarization, and the direction of propagation, and can thus be different for pump, signal, and idler photons. For dSPDC, in which the φ particle is massive and weakly interacting with matter the dispersion relation is the same as in vacuum,

$$k_\varphi = \sqrt{\omega_\varphi^2 - m_\varphi^2}. \quad (13)$$

Thus we can explicitly write the dispersion relation for each particle in this process:

$$k_p = n_p \omega_p, \quad (14)$$

$$k_s = n_s \omega_s \quad (15)$$

and

$$k_i = \begin{cases} n_i \omega_i & \text{for SPDC} \\ \sqrt{\omega_i^2 - m_\varphi^2} & \text{for dSPDC} \end{cases}. \quad (16)$$

where, again, the label “ i ” refers to an idler photon for SPDC and to the dark field φ for dSPDC. Note that k_i for SPDC not only has $m = 0$ but also takes into account the “strong (electromagnetic) coupling” with matter summarized by the refractive index n_i .

As a result, for SPDC we always have $k_i > \omega_i$ while for dSPDC $k_i < \omega_i$. Replacing these dispersion relations into (12) and using the first equation in (11) we obtain the phase matching relation of signal angle and frequency

$$\cos \theta_s = \frac{n_p^2 + \alpha_\omega^2 n_s^2 - \Xi^2}{2\alpha_\omega n_p n_s} \quad (17)$$

where we define

$$\alpha_\omega \stackrel{\text{def}}{=} \frac{\omega_s}{\omega_p} \quad (18)$$

and

$$\Xi \stackrel{\text{def}}{=} \frac{k_i}{\omega_p} = \begin{cases} n_i (1 - \alpha_\omega) & \text{for SPDC} \\ \sqrt{(1 - \alpha_\omega)^2 - \frac{m_\varphi^2}{\omega_p^2}} & \text{for dSPDC} \end{cases} \quad (19)$$

Equation (17) defines the phase space for (d)SPDC, along with the azimuthal angle ϕ_s . The idler angle, or that of the dark particle in the dSPDC case, is fixed in terms of the signal angle and frequency by requiring conservation of transverse momentum

$$\begin{aligned} \sin \theta_i &= \frac{k_s}{k_i} \sin \theta_s \\ \phi_i &= \phi_s + \pi \end{aligned} \quad (20)$$

where k_i is evaluated at a frequency of $\omega_i = \omega_p - \omega_s$, and k_s at the frequency ω_s according to the dispersion relation in Equations (15) and (16).

In the left panel of Figure 2 we show the allowed phase space in the α_ω - θ_s plane for SPDC and for dSPDC with both a massless and massive φ . Here we have chosen $n_p = 1.486$, $n_s = 1.658$ with $n_i = n_s$ in the SPDC case. These values were chosen to be constant with frequency and propagation direction, for simplicity and are inspired by the ordinary and extraordinary refractive indices in calcite and will be used as a benchmark in some of the examples below.

We see that phase matching is achieved in different regions of phase space for SPDC and its dark counterpart. In dSPDC, signal emission angles are restricted to near the forward region and in a limited range of signal frequencies. The need for more forward emission in dSPDC can be understood because φ effectively sees an index of refraction of 1. This implies it can carry less momentum for a given frequency, as compared to a photon which obeys $k = n\omega$. As a result, the signal photon must point nearly parallel to the pump, in order to conserve momentum (see Figure 2, right). An additional difference to notice is that, in contrast with the SPDC example shown, for a fixed signal emission angle there are two different signal frequencies that satisfy the phase matching in dSPDC. This will always be the case for dSPDC. Although SPDC can be of this form as well, typical refractive indices usually favor single solutions as shown for calcite.

1. Phase matching for colinear dSPDC

One case of particular interest is that of colinear dSPDC, in which the emission angle is zero, as would

occur in a single-mode fiber or a waveguide. For this case, so long as $n_s > n_p$, an axion mass below some threshold can be probed. Setting the emission angles to zero there are two solutions to the phase matching equations which give signal photon energies of

$$\alpha_\omega = \frac{(n_s n_p - 1) \pm \sqrt{(n_s - n_p)^2 - (n_s^2 - 1) \frac{m_\varphi^2}{\omega_p^2}}}{n_s^2 - 1} \quad (21)$$

The + solution above corresponds to the case where the φ particle is emitted in the forward direction whereas the - represents the case where it is emitted backwards. The signal frequency as a function of φ mass is shown in Figure 3 for the calcite benchmark. For the near-massless case, $m_\varphi \ll \omega_p$, a phase matching solution exists for $n_s \geq n_p$, giving

$$\frac{\omega_s}{\omega_p} = \frac{n_p \mp 1}{n_s \mp 1} \quad (22)$$

For calcite, we get $\omega_s = 0.739\omega_p$ and $\omega_s = 0.935\omega_p$ for forward and backward emitted axions respectively.

Of course, not any combination of n_p and n_s will allow to achieve phase matching in dSPDC. We will state here that $n_s > n_p$ is a requirement for phase matching to be possible for a massless φ and that $n_s - n_p$ must grow as m_φ grows. We will discuss these and other requirements for dSPDC searches in Section IV.

C. Thin planar layer of optical medium

We now consider the effects of a finite crystal. Specifically, we will assume that the optical medium is a planar thin layer² of optical material of length L along the pump propagation direction \hat{z} , and is infinite in transverse directions. In this case, the integral in Equation (8) is performed only over a finite range and the delta function is replaced by a sinc $x \equiv \sin x/x$ function

$$\int_{-L/2}^{L/2} dz e^{i\Delta k_z z} = L \text{sinc} \left(\frac{\Delta k_z L}{2} \right) \quad (23)$$

at the level of the amplitude. As advertised, this allows for momentum non-conservation with a characteristic width of order L^{-1} .

The fully differential rate will be proportional to the squared sinc function

$$\begin{aligned} \frac{d\Gamma}{d^3 k_p d^3 k_i} &\propto L^2 \text{sinc}^2 \left(\frac{\Delta k_z L}{2} \right) \delta^2(\Delta \mathbf{k}_T) \delta(\Delta \omega) \quad (24) \\ &\equiv \frac{d\hat{\Gamma}}{d^3 k_p d^3 k_i} \end{aligned} \quad (25)$$

where $\Delta \mathbf{k}_T$ is the momentum mismatch vector in the transverse directions. The constant of proportionality in Equation (24) will have frequency normalization

² The meaning of what constitutes the thin crystal layer limit in our context will be discussed in Section V.

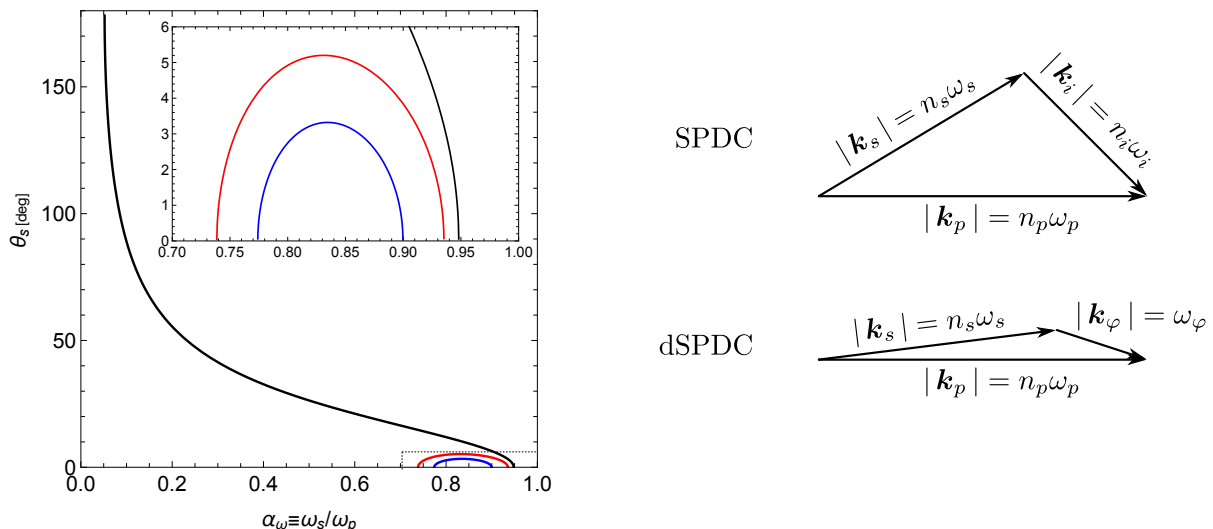


Figure 2: *Left*: The allowed phase space for SPDC (black), dSPDC with $m = 0$ (red), and dSPDC with $m = 0.1\omega_p$ (blue) shown as in the plane of signal emission angle as a function of frequency ratio α_ω . The indices of refraction here are $n_p = 1.658$ and $n_s = 1.486$ as an example, inspired by calcite. The inset shows a zoom-in of the dSPDC phase space. *Right*: Sketches depicting the momentum phase matching condition $\Delta\mathbf{k} = 0$ for SPDC and dSPDC, with massless φ . In both cases we take the same ω_p and ω_s . Due to the index of refraction for φ is essentially one, and that for the idler photon is larger (say ~ 1.5), phase matching in dSPDC has a smaller signal emission angle than that of SPDC.

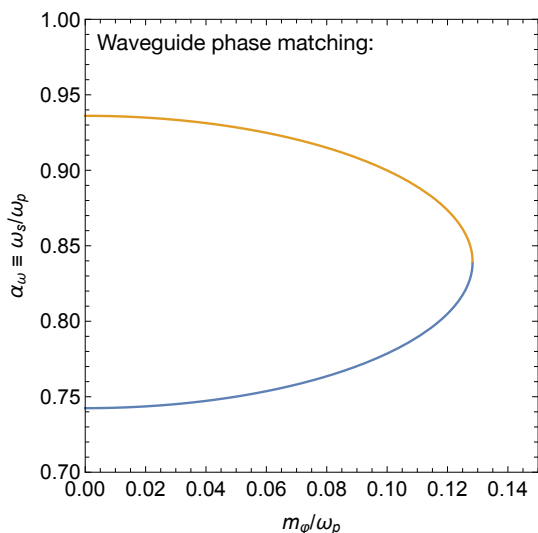


Figure 3: Solutions to the phase matching conditions for the colinear dark SPDC process for the signal photon energy as a function of the dark particle φ mass. This phase space is relevant for waveguide-based experiments. Both axes are normalized to the pump frequency. The two branches correspond to configurations in which φ is emitted forward (bottom) and backward (top).

factors of the form $(2\omega)^{-1}$ and the matrix element \mathcal{M} . The matrix element can also have non trivial angular dependence in θ as well as in ϕ , depending on the model and the optical medium properties. Note, however, that the current analysis for the phase space is model independent. We thus postpone the discussion of overall rates to Section V and to [17] and here we limit the study to the phase space distribution only. We will proceed with the defined phase space distribution $d\hat{\Gamma}$ in Equation (25), which we will now study.

One can trivially perform the integral over the d^3k_i which will effectively enforce Equation (20) for transverse momentum conservation, and set $|k_i|$ by conservation of energy. The argument of the sinc function is

$$\begin{aligned} \Delta k_z &= k_p - k_s \cos \theta_s - k_i \cos \theta_i \\ &= \omega_p \left(n_p - n_s \alpha_\omega \cos \theta_s \pm \sqrt{\Xi^2 - n_s^2 \alpha_\omega^2 \sin^2 \theta_s} \right) \end{aligned} \quad (26)$$

where in the second step we have used Equation (20) and the definitions of α_ω and Ξ in Equations (18) and (19). The \pm accounts for the idler or dark particle being emitted in the forward and backward direction respectively.

It is convenient to re-express the remaining three-dimensional phase space for (d)SPDC in terms of the signal emission angles θ_s and ϕ_s , and the signal frequency (or equivalently α_ω). Within our assumptions, the distribution in ϕ_s is flat. With respect to the polar angle and frequency we find

$$\frac{d^2\hat{\Gamma}}{d(\cos \theta_s) d\alpha_\omega} = \frac{2\pi\omega_p^3 \alpha_\omega^2 (1 - \alpha_\omega) n_s^3 \tilde{n}_i^2}{\sqrt{\Xi^2 - \alpha_\omega^2 n_s^2 \sin^2 \theta_s}} \sum_{\pm} L^2 \text{sinc}^2 \left[\left(n_p - n_s \alpha_\omega \cos \theta_s \pm \sqrt{\Xi^2 - n_s^2 \alpha_\omega^2 \sin^2 \theta_s} \right) \frac{\omega_p L}{2} \right] \quad (27)$$

where

$$\tilde{n}_i \stackrel{\text{def}}{=} \begin{cases} n_i & \text{for SPDC} \\ 1 & \text{for dSPDC} \end{cases}. \quad (28)$$

In Figure 4 we show the double differential distri-

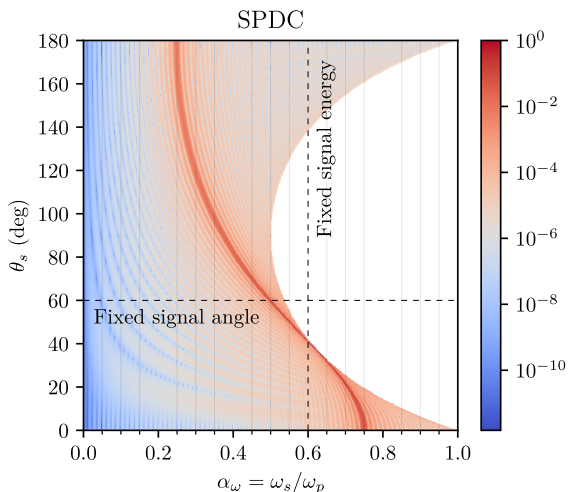


Figure 4: The phase space distribution $d^2\hat{\Gamma}/d(\cos\theta_s)d\alpha_\omega$ for SPDC in arbitrary units. We use $L = 1$, $\lambda_p = \frac{L}{10}$, $n_p = 2$ and $n_s = n_i = 4$. These parameters are unrealistic in practice, but allow for clear visualization of the distribution. Dashed lines show slices of fixed signal angle/energy.

bution $\hat{\Gamma}$ for SPDC, and in Figure 5 it is shown for dSPDC both for a massless and a massive φ . The distribution clearly peaks in regions of phase space that satisfy the phase matching conditions, those shown in Figure 2. To have a clearer view of the qualitative features in the distribution we picked somewhat exaggerated values for indices of refraction in these figures.

1. dSPDC Searches with Imaging or Spectroscopy

Though one can, in principle, measure both the angle and the energy of the signal photon, it is usually easier to measure either with a fixed angle or a fixed energy. For example, a CCD detector with a monochromatic filter can easily measure a single energy slice of this distribution, as shown in the vertical dashed line in Figure 4. Likewise, a spectrometer with no spatial resolution can measure a fixed angle slice of this distribution, as shown in the horizontal dashed line of Figure 4. An attractive choice for this is to look in the forward region, with an emission angle $\theta_s = 0$, which is the case for waveguides. For this colinear case we get a signal spectrum

$$\frac{d\hat{\Gamma}}{d\alpha_\omega} = \frac{2\pi\omega_p^3\alpha_\omega^2(1-\alpha_\omega)n_s^3\tilde{n}_i^2}{\Xi} \sum_{\pm} L^2 \text{sinc}^2\left(\frac{\Delta k_{z\pm}^{(0)}L}{2}\right) \quad (29)$$

where

$$k_{z\pm}^{(0)} = k_{zp} - k_{zs} - k_{zi}^{\pm} = \omega_p(n_p - n_s\alpha_\omega \pm \Xi) \quad (30)$$

is the momentum mismatch for colinear (d)SPDC. In some cases the colinear spectrum is dominated by just the forward emission of the idler/ φ , while in others there are two phase matching solutions which contribute similarly to the rate.

In Figure 6 we show two distributions, one for fixed signal frequency, and the other for a fixed signal angle, the latter in the forward direction. We see that both of these measurement schemes are able to distinguish the signal produced by different values of mass m_φ . Furthermore, in cases where the standard model SPDC process is a source of background, it can be separated from the dSPDC signal. As expected, in the forward measurement the dSPDC spectrum exhibits two peaks for the emission of φ in the forward or backward directions. It should be noted that the width of the highest peaks in these distributions decreases with crystal length L .

IV. OPTICAL MATERIALS FOR DARK SPDC

Having discussed the phase space distribution for dSPDC, we will now discuss which optical media are needed to open this channel, to enhance its rates, and, if possible, to suppress the backgrounds. A more complete estimate of the dSPDC rate will be presented in [17]. Here we will discuss the various features qualitatively to enable optimization of dSPDC searches.

A. Refractive Indices

As we discussed above, the refractive index of the optical medium plays a crucial role. It opens the phase space for the dSPDC decay and determines the kinematics of the process.

In order to enhance the dSPDC rate, it is always desirable to have a setup in which the dSPDC phase matching conditions which we discussed in Section III are accomplished. Since the left hand side of Equation (17) is the cosine of an angle, its right hand is restricted between ± 1 so

$$-1 < \frac{n_p^2 + \alpha_\omega^2 n_s^2 - \Xi^2}{2\alpha_\omega n_p n_s} < 1. \quad (31)$$

From this one finds that so long as $n_s > n_p$, there is a range of φ mass which can take part in dSPDC. As the difference $n_s - n_p$ is taken to be larger, a greater φ mass can be produced and larger opening angles θ_s can be achieved.

Using the inequalities in Equation (31) we can explore the range of desirable indices of refraction for a particular setup choice. For example, suppose we use monochromatic filter for the signal at half the energy of the pump photons, $\alpha_\omega = \frac{1}{2}$. Figure 7 shows in blue the region where the phase matching condition is satisfied for the SPDC process and in orange the region where the phase matching condition is satisfied for dSPDC. As can be seen, dSPDC is more restrictive in the refractive indices. Furthermore, typical SPDC experiments employ materials such as *beta barium borate* (BBO), *potassium dideuterium phosphate* (KDP) and *lithium triborate* (LBO) [19, 31–33] that do not allow the phase matching for dSPDC for this example.

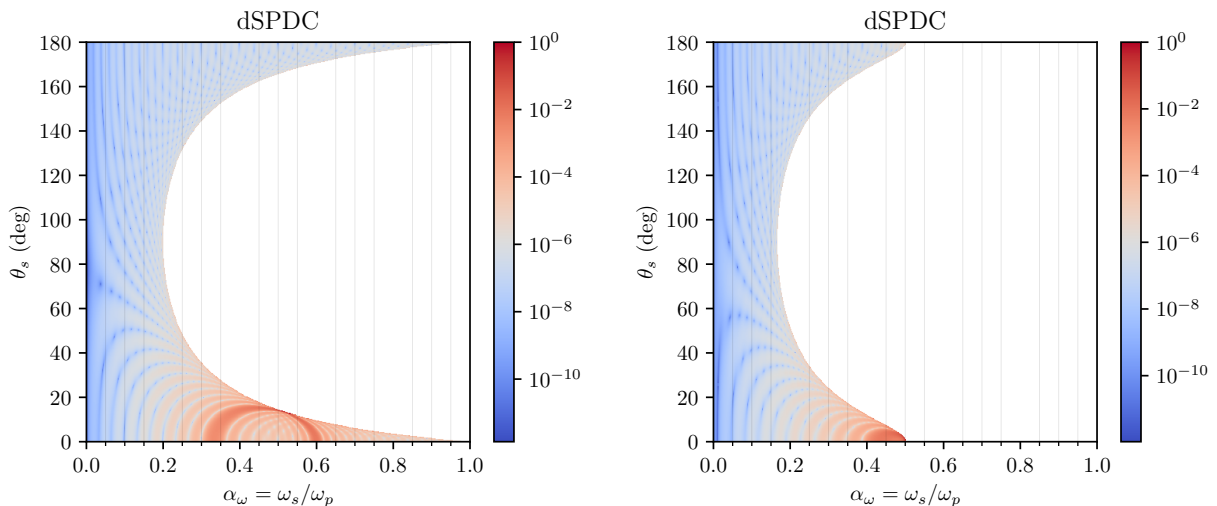


Figure 5: Phase space distribution $d^2\hat{\Gamma}/d(\cos\theta_s)d\alpha_\omega$ in arbitrary units for the dSPDC process for $m = 0$ (left) and $m = 0.5\omega_p$. The other parameters are as in Figure 4, with somewhat exaggerated indices of refraction to allow seeing the features in the distribution.

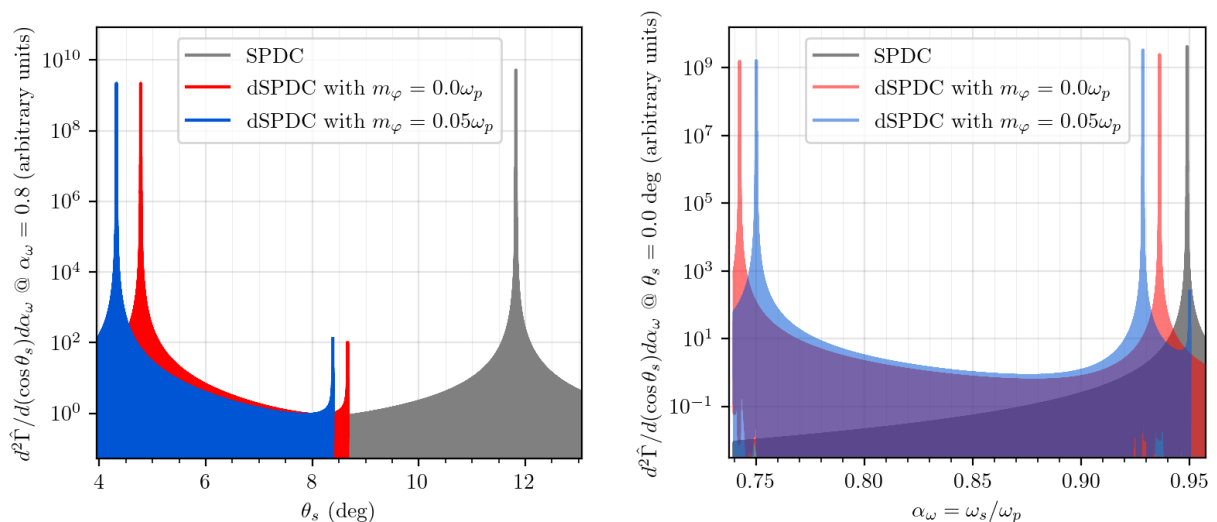


Figure 6: Slices of the phase space distributions for SPDC and for dSPDC with different choices of φ mass. On the left we show angle distributions with fixed signal frequency, and on the right we show frequency distributions for fixed signal angle. These distributions allow to separate SPDC backgrounds from the dSPDC signal, as well as the dSPDC signal for different values of m_φ . The distributions become narrower for thicker crystals, enhancing the signal to background separation power. For these distributions we used $L = 1$ cm, $\lambda_p = 400$ nm and for the refractive indices $n_p = 1.49$ and $n_s = n_i = 1.66$ inspired by calcite.

A second example which is well motivated is the forward region, namely $\theta_s = 0$. In this case phase matching can be achieved so long as

$$\frac{(n_s - n_p)^2}{n_s^2 - 1} \geq \frac{m_\varphi^2}{\omega_p^2}, \quad (32)$$

and $n_s > n_p$. We will investigate collinear dSPDC in greater detail in [17].

The dSPDC phase matching requirement $n_s > n_p$ can be achieved in practice by several effects. The most common one, employed in the majority of SPDC experiments, is birefringence [31, 33–35]. In this case the polarization of each photon is used to obtain a different refractive index. For instance, in calcite, the

ordinary and extraordinary polarizations have indices of refraction of $n_o = 1.658$ and $n_e = 1.486$. Taking the former to be the signal and the later for the pump, phase matching can be met for $m_\varphi < 0.16\omega_p$. Birefringence may also be achieved in single-mode fibers and waveguides with non-circular cross section, e.g. polarization-maintaining optical fibers [36]. Of course, the dependence of the refractive index on frequency may also be used to generate a signal-pump difference in n .

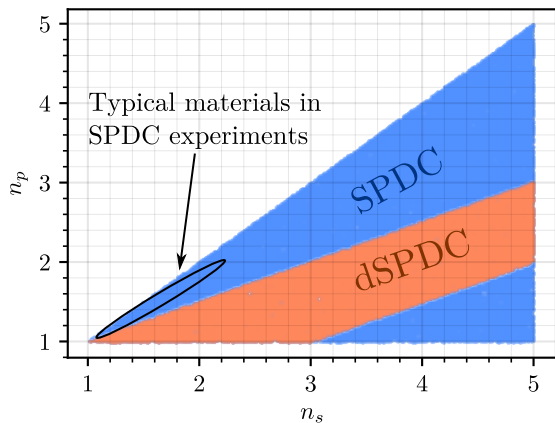


Figure 7: Regions in which the refractive indices n_p and n_s allow the phase matching with $\alpha_\omega \equiv \omega_s/\omega_p = \frac{1}{2}$ for the SPDC process (in this case assuming $n_i = n_s$) and dSPDC (in this case assuming $\frac{m}{\omega_p} \ll 1$).

B. Linear and Birefringent Media for Axions

Axion electrodynamics is itself a nonlinear theory. Therefore dSPDC with emission of an axion can occur in a perfectly linear medium. The optical medium is needed in order to satisfy the phase matching condition that cannot be satisfied in vacuum. Because the pump and signal photons in axion-dSPDC have different polarizations, a birefringent material can satisfy the requirement of $n_s > n_p$ and Equation (32). Because SPDC can be an important background to a dSPDC axion search, using a linear or nearly linear medium, where SPDC is absent is desirable. Interestingly, materials with a crystalline structure that is invariant under a mirror transformation $\mathbf{r} \rightarrow -\mathbf{r}$ will have a vanishing $\chi^{(2)}$ from symmetry considerations [37].

C. Longitudinal Susceptibility for Dark Photon Searches

As opposed to the axion case, a dSPDC process with a dark photon requires a nonlinear optical medium. As a result, SPDC can be a background to dSPDC dark photon searches. In SPDC, the pump, signal, and idler are standard model photons and their polarization is restricted to be orthogonal to their propagation. As a consequence, when one wants to enhance an SPDC process, the nonlinear medium is oriented in such a way that the second order susceptibility tensor $\chi^{(2)}$ can appropriately couple to the transverse polarization vectors of the pump, signal, and idler photons. The effective coupling between the modes in question is given by

$$\chi_{\text{SPDC}}^{(2)} \equiv \chi_{jkl}^{(2)} \varepsilon_j^p \varepsilon_k^s \varepsilon_l^i \quad (33)$$

with the ε being the (transverse) polarization vectors for the pump, signal and idler photons. These are spanned by $(1, 0, 0)$ and $(0, 1, 0)$ in a frame in which the respective photon is propagating in the \hat{z} direction.

In dSPDC with a dark photon there is an important difference. Because the dark photon is massive, it can

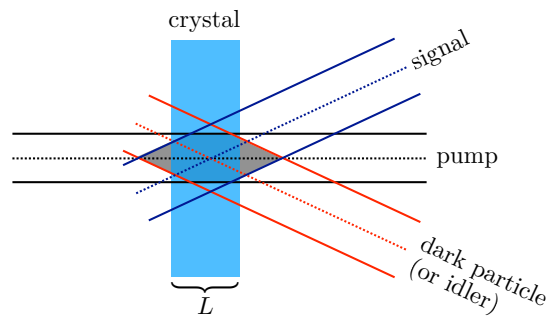


Figure 8: A sketch showing the overlap of the pump, signal, and dark particle (or idler) beams with the crystal. In general it is desirable to maximize the integration length which is defined by the overlap of the three beams and the crystal.

have a longitudinal polarization, $\varepsilon_l^{A'L} = (0, 0, 1)$. The crystal may be oriented to couple to this longitudinal mode, giving an effective coupling of

$$\chi_{A'L}^{(2)} \equiv \chi_{jkl}^{(2)} \varepsilon_j^p \varepsilon_k^s \varepsilon_l^{A'L} \quad (34)$$

Maximizing this coupling benefits the search both by enhancing signal and reducing background. The background is reduced because the SPDC effective coupling to transverse modes, Equation (33) is suppressed. The signal is enhanced because the coupling to the longitudinal polarization of the dark photon is suppressed by $m_{A'}/\omega$ rather than $(m_{A'}/\omega)^2$ [17, 28, 29, 38].

This motivates either non traditional orientation of nonlinear crystals, or identifying nonlinear materials that would usually be ineffective for SPDC. As an example in the first category, any material which is used for type II phase matching, in which the signal and idler have orthogonal polarization, can be rotated by 90 degrees to achieve a coupling of a longitudinal polarization to a pump and an idler. In the second category, material with $\chi^{(2)}$ tensors that are non-vanishing only in “maximally non-diagonal” \hat{x} - \hat{y} - \hat{z} elements, would obviously be discarded as standard SPDC sources, but can have an enhanced dSPDC coupling.

V. DARK SPDC SETUPS AND RATES

A precise estimate of the rate is beyond the scope of this work, and will be discussed in more detail in [17]. Here we will re-scale known rate formulae in order to examine the dependence of the rate on the geometric factors such as the pump power and beam area, the crystal length, and the area and angle from which signal is collected.

Consider the geometry sketched in Figure 8. A pump beam is incident on an optical element of length L along the the pump direction. The width of the pump beam is set by the laser parameters. The pump beam may consist of multiple modes, or can be guided in a fiber or waveguide [16] and in a single mode. The width and angle of the signal “beam” is set

by the apparatus used to collect and detect the signal. This too, can include collection of a single mode in a fiber (e.g. [19, 39]) or in multiple modes (as in the CCD example in the next section). In SPDC, when the idler photon may be collected the width and angle of the idler can also be set by a similar apparatus. However, in dSPDC (or in SPDC if we choose to only collect the signal) the φ beam is not a parameter in the problem. In this case we are interested in an inclusive rate, and would sum over a complete basis of idler beams. Such a sum will be performed in [17], but usually the sum will be dominated by a set of modes that are similar to those collected for the signal.

Generally, the signal rate will depend on all of the choices made above, but we can make some qualitative observations. The rate for SPDC and dSPDC will be proportional to an integral over the volume defined by the overlap of the three beams in Figure 8 and the crystal. When the length of the volume is set by the crystal, the process is said to occur in the “thin crystal limit”. In this limit, the beam overlap is roughly a constant over the crystal length and thus the total rate will grow with L . Since dSPDC is a rare process, we observe that taking the collinear limit of the process, together with a thicker crystal may allow for a larger integration volume and an enhanced rate.

The total rate for SPDC in a particular angle, integrated over frequencies, in the thin crystal limit is [17, 19],

$$\Gamma_{\text{SPDC}} \sim \frac{P_p \chi_{\text{eff}}^{(2)2} \omega_s \omega_i L}{\pi n_p n_s n_i A_{\text{eff}}} \quad (35)$$

where L is the crystal length, P_p is the pump power, A_{eff} is the effective beam area, and $\chi_{\text{eff}}^{(2)}$ is the effective coupling of Equation (33). A parametrically similar rate formula applies to SPDC in waveguides [16, 17]. The pump power here is the effective power, which may be enhanced within a high finesse optical cavity, e.g. [26]. The inverse dependence with effective area can be understood by since the interaction hamiltonian is proportional to electric fields, which grow for fixed power for a tighter spot. For “bulk crystal” setups a pair production rate of order few times 10^6 per mW of pump power per second is achievable [39] in the forward direction. In waveguided setups, in which the beams remain confined along a length of the order of a cm, production rates of order 10^9 pairs per mW per second are achievable in KTP crystals [16, 40], and rates of order 10^{10} were discussed for LN crystals [40]. Also noteworthy are cavity enhanced setups in which the effective pump power is increased by placing the device in an optical cavity, and/or OPOs, in which the signal photon is also a resonant mode, including compact devices with high conversion efficiencies, e.g [41–44].

An important scaling of this rate is the L/A_{eff} dependence. This scaling applies for dSPDC rates discussed below. Within the thin crystal limit one can thus achieve higher rates with: (a) a smaller beam spot, and (b) a thicker crystal. It should be noted that for collinear SPDC, the crystal may be in the “thin limit” even for thick crystals (see Figure 8 and imagine zero signal and idler emission angle).

A. Dark Photon dSPDC Rate

The dSPDC rate into a dark photon with longitudinal polarization, A'_L , can similarly be written as a simple re-scaling of the expression above

$$\Gamma_{\text{dSPDC}}^{(A'_L)} \sim \epsilon^2 \frac{m_{A'}^2}{\omega_{A'}^2} \frac{P_p \chi_{A'_L}^{(2)2} \omega_s \omega_{A'} L}{n_p n_s A_{\text{eff}}} \quad (36)$$

where the effective coupling $\chi_{A'_L}^{(2)}$ is defined in Equation (34). This is valid in regions where the dark photon mass is smaller than the pump frequency, such that the produced dark photons are relativistic and have a refractive index of 1. Using the optimistic waveguide numbers above as a placeholder, assuming an optimized setup with similar $\chi^{(2)}$, the number of events expected after integrating over a time t_{int} are

$$N_{\text{events}}^{(A'_L)} \sim 10^{21} \left(\epsilon^2 \frac{m_{A'}^2}{\omega_{A'}^2} \right) \left(\frac{P_p}{\text{Watt}} \right) \left(\frac{L}{\text{m}} \right) \left(\frac{t_{\text{int}}}{\text{year}} \right). \quad (37)$$

The current strongest lab-based limit is for dark photon masses of order 0.1 eV is set by the ALPS experiment at $\epsilon \sim 3 \times 10^{-7}$. For this dark photon mass $m_{A'} \sim 0.1 \omega_p$, the $m_{A'}/\omega_{A'}$ term does not represent a large suppression. In this case of order 10 dSPDC events are produced in a day in a 1 cm crystal with a Watt of pump power with the assumptions above. This implies that a relatively small dSPDC experiment with an aggressive control on backgrounds could be used to push the current limits on dark photons.

Improving the limits from solar cooling, for which $\epsilon m_{A'}/\omega_{A'}$ is constrained to be smaller, would represent an interesting challenge. Achieving ten events in a year of running requires a Watt of power in a waveguide greater than 10 meters (or a shorter waveguide with higher stored power, perhaps using a Fabri-Perot setup). Interestingly, in terms of system size, this is still smaller than the ALPS-II experiment which would reach 100 meters in length and an effecting power of a hundred kW. This is because LSW setups require both production and detection, with limits scaling as ϵ^4 .

B. Axion dSPDC Rate

A similar rate expression can be obtained for axion-dSPDC

$$\Gamma_{\text{dSPDC}}^{(\text{axion})} \sim \frac{P_p g_{a\gamma\gamma}^2 \omega_s L}{\omega_{\text{axion}} n_p n_s A_{\text{eff}}} \quad (38)$$

where the different scaling with the frequency of the dark field is due to the different structure of the dSPDC interaction (recall that $\chi^{(2)}$ carries a mass dimension of -2 while the axion photon coupling’s dimension is -1). Optimal SPDC (dSPDC) rates are achieved in waveguides in which the effective area is of order the squared wavelength of the pump and signal light. Assuming a (linear) birefringent material that can achieve dSPDC phase matching for an axion the

| | Dark Photon ($m_{A'} = 0.1$ eV) | Axion-like particle ($m_a = 0.1$ eV) |
|---------------------|--|--|
| Current lab limit | $\epsilon < 3 \times 10^{-7}$ | $g_{a\gamma} < 10^{-6} \text{ GeV}^{-1}$ |
| Example dSPDC setup | $P_p = 1$ W $L = 1$ cm $\Gamma = 10/\text{day}$ | $P_p = 1$ kW $L = 10$ m $\Gamma = 10/\text{day}$ |
| Current Solar limit | $\epsilon < 10^{-10}$ | $g_{a\gamma} < 10^{-10} \text{ GeV}^{-1}$ |
| Example dSPDC setup | $P_p = 1$ W $L = 10$ m $\Gamma = 10/\text{year}$ | $P_p = 100$ kW $L = 100$ m $\Gamma = 10/\text{year}$ |

Table I: Current lab-based and Solar-based based limits on the couplings of dark photons and axion-like particles with a benchmark mass of 0.1 eV. For each limit we show the parameters of an example dSPDC in a waveguide and the rate it would produce for couplings that would produce the specified benchmark rate with the corresponding coupling. The pump power is an effective power which can include an enhancement by an optical cavity setup. For dark photon rates we assume a nonlinearity of the same order found in KTP crystals.

number of signal event scales as

$$N_{\text{events}}^{(\text{axion})} \sim 40 \left(\frac{g_{a\gamma}}{10^{-6} \text{ GeV}^{-1}} \right)^2 \left(\frac{P_p}{\text{Watt}} \right) \left(\frac{L}{\text{m}} \right) \left(\frac{t_{\text{int}}}{\text{year}} \right). \quad (39)$$

This rate suggests a dSPDC setup is promising in setting new lab-based limits on ALPs. For example, a 10 meter birefringent single mode fiber with kW of pump power will generate of order 10 events per day for couplings of order 10^{-7} GeV^{-1} . To probe beyond the CAST limits in $g_{a\gamma}$ may be possible and requires a larger setup, but not exceeding the scale, say, of ALPS-II. In a 100 meter length and an effective pump power of 100 kW, a few dSPDC signal events are expected in a year.

Maintaining a low background, would of course be crucial. We note, however, that optical fibers are routinely used over much greater distances, maintaining coherence (e.g. [5]), and an optimal setup should be identified.

C. Backgrounds to dSPDC

There are several factors that should be considered for the purpose of reducing backgrounds to SPDC:

- **Crystal Length and Signal bandwidth:** In addition to the growth of the signal rate, the signal bandwidth in many setups will decrease with L . If this is achieved the signal to background ratio in a narrow band around the dSPDC phase matching solutions will scale as L^2 .
- **Timing:** The dSPDC signal consists of a single photon whereas SPDC backgrounds will consist of two coincident photons. Backgrounds can be reduced using fast detectors and rejecting coincidence events.
- **Optical material:** As pointed out in Section IV, linear birefringent materials can be used to reduce SPDC backgrounds to axion searches. Nonlinear materials with a $\chi^{(2)}$ tensor which couples purely to longitudinal polarizations may be used to enhance dark photon dSPDC events

without enhancing SPDC. This technique to reduce SPDC may also be used in axion searches.

- **Detector noise and optical impurities:** Sources of background which may be a limiting factor for dSPDC searches include detector noise, as well as scattering of pump photons off of impurities in the optical elements and surfaces. The Skipper CCD, one example of a detector technology with low noise, will be discussed in the next section.

An optimal dSPDC based search for dark particles will likely consider these factors, and is left for future investigation.

VI. EXPERIMENTAL PROOF OF CONCEPT

In this section we present an experimental SPDC angular imaging measurement with high resolution employing a Skipper CCD and a BBO nonlinear crystal. In this setup and for the chosen frequencies, dSPDC phase matching is not achievable at any emission angle. Instead, this experiment serves as a proof of concept for the high resolution imaging technique.

Imaging the dSPDC requires the detection of single photons with low noise and with high spatial and/or energy resolution. A technology that can achieve this is the Skipper CCD which is capable of measuring the charge stored in each pixel with single electron resolution [18], ranging from very few electrons (0, 1, 2, ...) up to more than a thousand (1000, 1001, 1002, ...) [45]. This unique feature combined with the high spatial resolution typical of a CCD detector makes this technology very promising for the detection of small optical signals with a very high spatial resolution.

A. Description of the experimental setup

With the aim of comparing the developed phase space model against real data, the system depicted

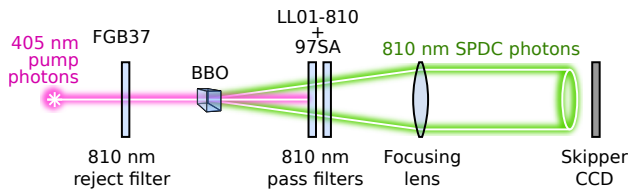


Figure 9: Pictorial representation of the experimental setup implemented in the lab. A 405 nm diode laser was used as a source of pump photons. The beam passes through a 810 nm rejection filter, then through the BBO crystal, after this through two 810 nm band pass filters, a focusing lens and finally the SPDC photons reach the CCD detector.

in Figure 9 was set up. A source of entangled photons that employs SPDC, which is part of a commercial system³, was used. Two type I nonlinear BBO crystals are used as a high efficient source of entangled photons [31]. This pre-assembled source can be seen in Figure 10. However, in this work, we did not take advantage of the polarization entanglement, we only use the energy-momentum conservation to get spatially correlated twin photons. In addition to the original design, we added a Thorlabs FGB37 filter after the laser to remove a small 810 nm component coming along with the pump beam. After the BBO crystal, where the SPDC process occurs, two additional 810 nm band pass filters (one Semrock Brighline LL01-810 and one Asahi Spectra 97SA) were placed to prevent the 405 nm pump beam from reaching the detector. We also placed a lens at its focal distance from the BBO to prevent the SPDC cone from spreading during its travel to the CCD (see Figure 9). Thus, we got the SPDC ring projected on the CCD surface with a radius of 110 pixel, which corresponds to 1650 μm . This setup is also part of a research where the novel features of Skipper CCD [18] are being tested for Quantum Imaging. The capability of Skipper-CCD to reduce the readout noise as low as desired taking several samples of the charge in each pixel was not used in this work to acquire data, but it was for the calibration. Details about the same detector used here can be found in reference [45].

We used an absolute calibration between the Analog to Digital Units (ADU) measured by the amplifier from the CCD and the number of electrons in each pixel, possible with the Skipper-CCD, which was previously carried out for this system [45]. Thus, we reconstructed the number of photons per pixel, since at 810 nm it can be assumed that one photon creates at most one electron, by reason of its energy is 0.43 eV above the silicon band gap (1.1 eV). The factor affecting that relationship is the efficiency which -besides being very high ($\sim 90\%$) at this wavelength- is pretty uniform over the entire CCD surface [47].

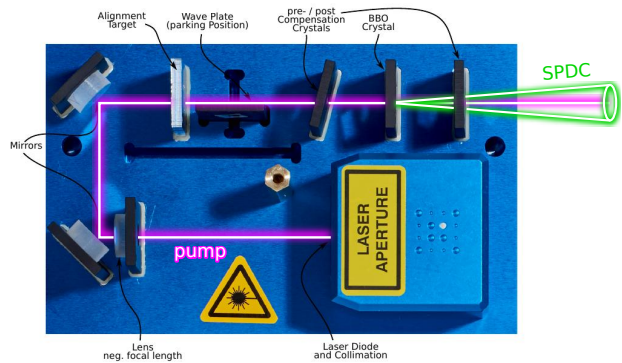


Figure 10: Picture of the source of entangled photons which is a part of a commercial system. The FGB37 filter shown in Figure 9 was placed just after the laser aperture. All the other components were placed outside this device. Figure adapted from [46].

B. Results

Using the setup previously described, 400 images with 200s exposure each were averaged to produce the data used for comparison with the model. Thus, we reduced a factor twenty the uncertainty in the expected number of photons in each pixel and drastically reduced the dark counts coming from random background. This significantly improved the identification of minima between rings, which results to be crucial to compare the experimental data with the presented theory.

Figure 11 presents the averaged image of the SPDC ring coming out of the BBO crystal. The main ring is clearly visible, as well as many secondary maxima and minima. The angular coordinates θ and ϕ were indicated on the image. It has to be noted that the angular coordinates used in the previous sections are the ones inside the optical medium. Since the CCD detector is outside the BBO crystal, Snell's law must be used to relate the angles inside and outside the nonlinear crystal. Specifically, for the θ coordinate this is

$$\theta = \arcsin\left(\frac{\sin \Theta}{n}\right)$$

where θ is the angle inside the optical medium in which the SPDC process occurs, Θ is the angle outside the optical medium and n is the refractive index. In this work we apply the transformation to refer all angles to those inside the optical medium in which the interaction occurs.

As can be seen in the image, even though it is possible to see many of the maxima and minima, there is a non uniform background component produced by reflections and other imperfections of the experimental configuration. The current implementation of our setup has some mechanical limitations that make hard to isolate, measure and remove this non-uniform background component. Still, this image can be used to compare the theory with the experiment, so the profile of the intensity distribution along the blue dashed line shown in Figure 11 was extracted and plotted against

³ <https://www.qutools.com/qued/>

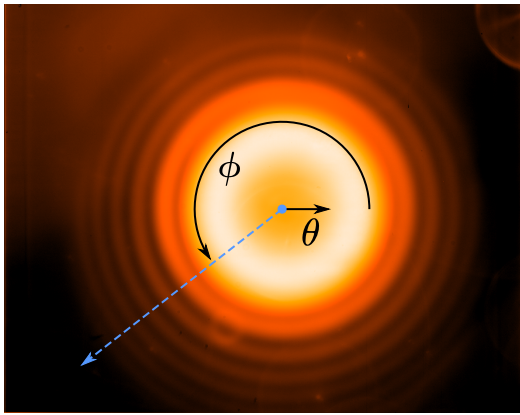


Figure 11: Average of 400 images with 200s exposure each to the SPDC photons each using the setup depicted in Figure 9. The angular coordinates θ and ϕ are indicated in the figure. The blue dashed line was used to extract the data profile shown in Figure 12.

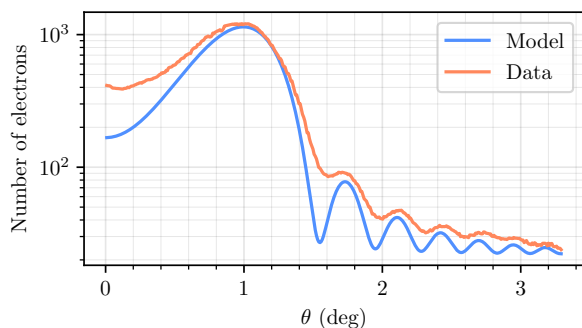


Figure 12: Experimental intensity profile for the SPDC ring along the blue dashed line in Figure 11 compared with theoretical distribution. The y axis scale is the number of electrons in each pixel of the CCD detector obtained via the absolute Skipper-CCD calibration described.

the model. This plot is shown in Figure 12. Some comments about this plot:

- A uniform background component was added to the model.
- The transmittance curve of the 810 nm filters provided by the manufacturers was taken into account.

So, to be specific, the plot in Figure 12 uses as model the intensity profile given by

$$I_{\text{model}}(\theta) = I_0 \int \frac{d^2\hat{\Gamma}}{d(\cos\theta_s)d\alpha_\omega} F(\alpha_\omega) d\alpha_\omega + I_1$$

where I_0 and I_1 are real numbers fitted, $\frac{d^2\hat{\Gamma}}{d(\cos\theta_s)d\alpha_\omega}$ is given by Equation (27) and $F(\alpha_\omega)$ is the transmittance of the filters as provided by the manufacturers, which is a sharp peaked function centered at 810 nm with a pass band of 10 nm width.

For the parameters of the distribution $\hat{\Gamma}$, we used:

- 405 nm for the pump wavelength as provided by the manufacturer of the laser,

- the refractive indices for the BBO crystal were taken from <https://refractiveindex.info/>⁴
- and the crystal length was assumed to be $L = 1.14$ mm after fine tuning⁵.

We had to perform a fine tuning of $n_s - n_p$ too (since signal and idler have the same frequency and angle then $n_s = n_i$). The model is very sensitive to this difference, and this quantity depends on factors such as the temperature of the BBO and its precise orientation in space, which were not measured. So it is not surprising that we had to perform this fine tuning on $n_s - n_p$. The final values used for the refractive indices were $n_p \approx 1.66082$ and $n_s = n_i \approx 1.66107$. Although this fine tuning had to be done, all parameters are very well within expected values.

As seen both in Figures 11 and 12 the phase space factor, studied in previous sections, is the dominant modulation in the distribution of photons for the SPDC process in our setup. Even though there is a non negligible background component, it is evident the dependence $I \sim \text{sinc}^2(\theta^2)$ for small values of θ predicted by Equation (27).

VII. DISCUSSION

We have presented a new method to search for new light and feebly coupled particles, such as axion-like particles and dark photons. The dSPDC process allows to tag the production of a dark state as a pump photon down-converts to a signal photon and a “dark idler” φ , in close analogy to SPDC. We have shown that the presence of indices of refraction that are different than 1 open the phase space for the decay, or down conversion, of the massless photon to the signal plus the dark particle, even if φ has a mass. This type of search has a parametric advantage over light shining through wall setups since it only requires producing the axion or dark photon, without a need to detect it again. Precise sensitivity calculations for dSPDC with Dark Photon and Axion cases that can be achieved through this method are ongoing [17].

The commonplace use of optics in telecommunications, imaging and in quantum information science, as well as the development of advanced detectors, can thus be harnessed to search for dark sector particles. Increasing dSPDC signal rates will require high laser power, long optical elements. Enhancing the signal and suppressing SPDC backgrounds also requires

⁴ The extraordinary refractive index was taken from <https://refractiveindex.info/?shelf=main&book=BaB204&page=Tamosauskas-e> (Tamošauskas et al., 2018) and the ordinary refractive index from <https://refractiveindex.info/?shelf=main&book=BaB204&page=Eimerl-o> (Eimerl et al., 1987).

⁵ It was not possible to obtain precise information of the dimensions of the crystal from the manufacturer. Furthermore, the length of the crystal is not easy to measure with our current implementation without breaking the SPDC source shown in Figure 10. So we decided to use a “reasonable value” and fine tune it.

identifying the right optical media for the search. Axion searches would benefit from optically linear and birefringent materials, with greater birefringence allowing to search for higher axion masses. Searches for dark photons would benefit from strongly nonlinear materials that are capable of coupling to a longitudinal polarization. This, in turn, motivated either non-conventional optical media, or using conventional crystals that are oriented by a 90° rotation from that which is desired for SPDC. Enhancing the effective pump power with an optical cavity is a straightforward way to enhance the dSPDC rate. We leave the exploration of a “doubly resonant” OPO setup in which the signal is also a cavity eigenmode (in parallel with [26]) for future work. Finally, detection of rare signal events requires sensitive single photon detectors with high spatial and/or frequency resolution.

We also performed an experimental demonstration of the one of the setups discussed using a Skipper CCD for SPDC imaging. The setup we used for this demonstration was adapted from one designed to enforce SPDC and thus does not open dSPDC phase space. We show that the Skipper technology allows one to measure with high accuracy. Thus, quantum teleportation methods or ghost imaging of dark sector particles achieved through phase space engineering is a very promising technique for future explorations of dark sector parameter spaces.



Acknowledgments: We would like to thank Joe Chapman, Paul Kwiat, and Neal Sinclair for informative discussions. This work was funded by a DOE QuantISED grant.

-
- [1] A. Furusawa. Unconditional Quantum Teleportation. *Science*, 282(5389):706–709, October 1998.
 - [2] D. Boschi, S. Branca, F. De Martini, L. Hardy, and S. Popescu. Experimental Realization of Teleporting an Unknown Pure Quantum State via Dual Classical and Einstein-Podolsky-Rosen Channels. *Physical Review Letters*, 80(6):1121–1125, February 1998.
 - [3] Dik Bouwmeester, Jian-Wei Pan, Klaus Mattle, Manfred Eibl, Harald Weinfurter, and Anton Zeilinger. Experimental quantum teleportation. *Nature*, 390(6660):575–579, December 1997.
 - [4] Charles H. Bennett, Gilles Brassard, Claude Crepeau, Richard Jozsa, Asher Peres, and William K. Wootters. Teleporting an unknown quantum state via dual classical and Einstein-Podolsky-Rosen channels. *Physical Review Letters*, 70(13):1895–1899, March 1993.
 - [5] Raju Valivarthi, Samantha Davis, Cristian Pena, Si Xie, Nikolai Lauk, Lautaro Narvaez, Jason P. Allmaras, Andrew D. Beyer, Yewon Gim, Meraj Hussein, George Iskander, Hyunseong Linus Kim, Boris Korzh, Andrew Mueller, Mandy Rominsky, Matthew Shaw, Dawn Tang, Emma E. Wollman, Christoph Simon, Panagiotis Spentzouris, Neil Sinclair, Daniel Oblak, and Maria Spiropulu. Teleportation Systems Towards a Quantum Internet. *arXiv e-prints*, page arXiv:2007.11157, July 2020.
 - [6] Interaction.
 - [7] C. K. Hong and L. Mandel. Theory of parametric frequency down conversion of light. *Physical Review A*, 31(4):2409–2418, 1985.
 - [8] J. A. Giordmaine and Robert C. Miller. Tunable Coherent Parametric Oscillation in LiNbO₃ at Optical Frequencies. *Physical Review Letters*, 14(24):973–976, June 1965.
 - [9] R. Essig and et al. Dark Sectors and New, Light, Weakly-Coupled Particles. *arXiv:1311.0029 [astro-ph, physics:hep-ex, physics:hep-ph]*, October 2013. arXiv: 1311.0029.
 - [10] F. Hoogeveen and T. Ziegenhagen. Production and detection of light bosons using optical resonators. *Nucl. Phys. B*, 358:3–26, 1991.
 - [11] Jessica Goodman, Masahiro Ibe, Arvind Rajaraman, William Shepherd, Tim M.P. Tait, and Hai-Bo Yu. Constraints on Light Majorana dark Matter from Colliders. *Phys. Lett. B*, 695:185–188, 2011.
 - [12] Yang Bai, Patrick J. Fox, and Roni Harnik. The Tevatron at the Frontier of Dark Matter Direct Detection. *JHEP*, 12:048, 2010.
 - [13] Jessica Goodman, Masahiro Ibe, Arvind Rajaraman, William Shepherd, Tim M.P. Tait, and Hai-Bo Yu. Constraints on Dark Matter from Colliders. *Phys. Rev. D*, 82:116010, 2010.
 - [14] Patrick J. Fox, Roni Harnik, Joachim Kopp, and Yuhsin Tsai. Missing Energy Signatures of Dark Matter at the LHC. *Phys. Rev. D*, 85:056011, 2012.
 - [15] T. Aaltonen et al. A Search for dark matter in events with one jet and missing transverse energy in $p\bar{p}$ collisions at $\sqrt{s} = 1.96$ TeV. *Phys. Rev. Lett.*, 108:211804, 2012.
 - [16] Marco Fiorentino, Sean M. Spillane, Raymond G. Beausoleil, Tony D. Roberts, Philip Battle, and Mark W. Munro. Spontaneous parametric down-conversion in periodically poled KTP waveguides and bulk crystals. *Optics Express*, 15(12):7479–7488, June 2007.
 - [17] Juan Estrada, Roni Harnik, Dario Rodrigues, and Matias Senger. New Particle Searches with Nonlinear Optics. *In preparation*.
 - [18] Javier Tiffenberg, Miguel Sofo-Haro, Alex Drlica-Wagner, Rouven Essig, Yann Guardincerri, Steve Holland, Tomer Volansky, and Tien-Tien Yu. Single-electron and single-photon sensitivity with a silicon Skipper CCD. *Physical Review Letters*, 119(13):131802, September 2017. arXiv: 1706.00028.
 - [19] Alexander Ling, Antia Lamas-Linares, and Christian Kurtsiefer. Absolute emission rates of Spontaneous Parametric Down Conversion into single transverse Gaussian modes. *Physical Review A*, 77(4):043834, April 2008. arXiv: 0801.2220.
 - [20] James Schneeloch and John C Howell. Introduction to the transverse spatial correlations in spontaneous parametric down-conversion through the biphoton birth zone. *Journal of Optics*, 18(5):053501, 2016.
 - [21] P.A. Zyla et al. Review of Particle Physics. *PTEP*, 2020(8):083C01, 2020.
 - [22] Georg G. Raffelt. Astrophysical methods to constrain axions and other novel particle phenomena. *Phys. Rept.*, 198:1–113, 1990.
 - [23] V. Anastassopoulos et al. New CAST Limit on the Axion-Photon Interaction. *Nature Phys.*, 13:584–590, 2017.

- [24] Federico Della Valle, Aldo Ejlli, Ugo Gastaldi, Giuseppe Messineo, Edoardo Milotti, Ruggero Pengo, Giuseppe Ruoso, and Guido Zavattini. The PVLAS experiment: measuring vacuum magnetic birefringence and dichroism with a birefringent Fabry–Perot cavity. *Eur. Phys. J. C*, 76(1):24, 2016.
- [25] R. Ballou et al. New exclusion limits on scalar and pseudoscalar axionlike particles from light shining through a wall. *Phys. Rev. D*, 92(9):092002, 2015.
- [26] Klaus Ehret et al. Resonant laser power build-up in ALPS: A ‘Light-shining-through-walls’ experiment. *Nucl. Instrum. Meth. A*, 612:83–96, 2009.
- [27] Robin BÄhre et al. Any light particle search II — Technical Design Report. *JINST*, 8:T09001, 2013.
- [28] Haipeng An, Maxim Pospelov, and Josef Pradler. New stellar constraints on dark photons. *Phys. Lett. B*, 725:190–195, 2013.
- [29] Haipeng An, Maxim Pospelov, and Josef Pradler. Dark Matter Detectors as Dark Photon Helioscopes. *Phys. Rev. Lett.*, 111:041302, 2013.
- [30] David Tong. *Quantum Field Theory*. <http://www.damtp.cam.ac.uk/user/tong/qft.html>.
- [31] Paul G. Kwiat, Edo Waks, Andrew G. White, Ian Appelbaum, and Philippe H. Eberhard. Ultra-bright source of polarization-entangled photons. *Physical Review A*, 60(2):R773–R776, August 1999. arXiv: quant-ph/9810003.
- [32] Christophe Couteau. Spontaneous parametric down-conversion. *Contemporary Physics*, 59(3):291–304, July 2018.
- [33] N. Boeuf. Calculating characteristics of noncollinear phase matching in uniaxial and biaxial crystals. *Optical Engineering*, 39(4):1016, April 2000.
- [34] Paul-Antoine Moreau, Ermes Toninelli, Thomas Gregory, and Miles J. Padgett. Imaging with quantum states of light. *Nature Reviews Physics*, 1(6):367–380, June 2019.
- [35] S. Magnitskiy, D. Frolovtsev, V. Firsov, P. Gostev, I. Protsenko, and M. Saygin. A SPDC-Based Source of Entangled Photons and its Characterization. *Journal of Russian Laser Research*, 36(6):618–629, November 2015.
- [36] J. Noda, K. Okamoto, and Y. Sasaki. Polarization-maintaining fibers and their applications. *Journal of Lightwave Technology*, 4(8):1071–1089, 1986.
- [37] Robert W. Boyd. *Nonlinear optics*. Academic Press, Amsterdam ; Boston, 3rd ed edition, 2008.
- [38] Peter W. Graham, Jeremy Mardon, Surjeet Rajendran, and Yue Zhao. Parametrically enhanced hidden photon search. *Phys. Rev. D*, 90(7):075017, 2014.
- [39] Ryan S. Bennink. Optimal Co-linear Gaussian Beams for Spontaneous Parametric Down-Conversion. *Physical Review A*, 81(5):053805, May 2010. arXiv: 1003.3810.
- [40] Sean M. Spillane, Marco Fiorentino, and Raymond G. Beausoleil. Spontaneous parametric down conversion in a nanophotonic waveguide. *Optics Express*, 15(14):8770–8780, July 2007.
- [41] J. U. FÄErst, D. V. Strekalov, D. Elser, A. Aiello, U. L. Andersen, Ch. Marquardt, and G. Leuchs. Low-Threshold Optical Parametric Oscillations in a Whispering Gallery Mode Resonator. *Physical Review Letters*, 105(26):263904, December 2010.
- [42] T. Beckmann, H. Linnenbank, H. Steigerwald, B. Sturman, D. Haertle, K. Buse, and I. Breunig. Highly Tunable Low-Threshold Optical Parametric Oscillation in Radially Poled Whispering Gallery Resonators. *Physical Review Letters*, 106(14):143903, April 2011.
- [43] Christoph S. Werner, Karsten Buse, and Ingo Breunig. Continuous-wave whispering-gallery optical parametric oscillator for high-resolution spectroscopy. *Optics Letters*, 40(5):772, March 2015.
- [44] Juanjuan Lu, Ayed Al Sayem, Zheng Gong, Joshua B. Surya, Chang-Ling Zou, and Hong X. Tang. Ultralow-threshold thin-film lithium niobate optical parametric oscillator, 2021.
- [45] Dario Rodrigues, Kevin Andersson, Mariano Cababie, Andre Donadon, Gustavo Cancelo, Juan Estrada, Guillermo Fernandez-Moroni, Ricardo Piegaiia, Matias Senger, Miguel Sofo Haro, et al. Absolute measurement of the fano factor using a skipper-ccd. *arXiv preprint arXiv:2004.11499*, 2020.
- [46] qutools. quED.
- [47] C.J. Bebek, J.H. Emes, D.E. Groom, S. Haque, S.E. Holland, P.N. Jelinsky, A. Karcher, W.F. Kolbe, J.S. Lee, N.P. Palaio, D.J. Schlegel, G. Wang, R. Groulx, R. Frost, J. Estrada, and M. Bonati. Status of the CCD development for the dark energy spectroscopic instrument. *Journal of Instrumentation*, 12(04):C04018–C04018, apr 2017.